Ag and Cu doping and their effects on the thermoelectric properties of β-Zn_4Sb_3

Mian Liu, Xiaoying Qin,* Changsong Liu, Lin Pan, and Hongxing Xin
Key Laboratory of Materials Physics, Institute of Solid State Physics, Chinese Academy of Sciences, P.O. Box 1129, Hefei 230031, People's Republic of China

(Received 11 November 2009; revised manuscript received 26 May 2010; published 29 June 2010)

The measurements of electrical resistivity and Seebeck coefficients of Ag- and Cu-doped compounds β-$(Zn_{1-x}M_x)_4Sb_3$ (M=Ag,Cu; x=0,0.0025,0.005,0.01) were carried out, and the results indicated that both their resistivity and Seebeck coefficients increase first ($x \leq 0.0025$ for Ag and $x \leq 0.005$ for Cu) and then decrease obviously with further increase in their doping content. Correspondingly, hole concentration behaviors in the opposite way. In terms of the one vacancy-two interstitial Zn atom model: $A_{11}BCSb_{10}$ and two-vacancy-three-interstitial Zn atom model: $A_{10}BCDSb_{10}$ (here A is normal Zn atom and B, C, and D interstitial Zn atoms) proposed by Cargnoni *et al.* [Chem. Eur. J. **10**, 3861 (2004)], first-principles calculations were performed on the occupation options of Ag and Cu atoms in disordered β-Zn_4Sb_3. The results indicated that both Ag and Cu atoms occupy preferentially the Zn vacancies in normal sites. Subsequently, Ag and Cu atoms will substitute for interstitial atoms D (for Ag) and B (for Cu). The calculations also showed that as Ag and Cu atoms fill Zn vacancies they play the role of donors, leading to a decrease in hole concentration; while Ag and Cu atoms replace the interstitial atoms they act as acceptors resulting in an increase in hole concentration, which are in good agreement with the nonmonotonous change behavior in the transport properties and Hall carrier concentrations observed experimentally. In addition, calculations revealed that Cu instead of Ag can also fill the Zn vacancies with smaller volumes and Cu doping nearly always has lower formation energies than Ag, which could give a reasonable explanation for the higher solubility of Cu than that of Ag in β-Zn_4Sb_3.

DOI: 10.1103/PhysRevB.81.245215 PACS number(s): 71.20.Nr, 71.20.Lp, 72.20.Pa, 72.15.Jf

I. INTRODUCTION

In the past decade, thermoelectric materials have been attracting many theoretical and practical interests owing to their potential applications in energy conversion and power generation.[1–6] Among the good thermoelectric materials, β-Zn_4Sb_3 emerged as a prospective thermoelectric material for commercial application in the moderate temperature range because of the prominent high thermoelectric performance, ZT=1.3 at 670 K [$ZT=S^2T/\rho\lambda$, here S is the Seebeck coefficient, ρ is the electrical resistivity, $\lambda(=\lambda_L+\lambda_C)$ is thermal conductivity with both lattice (λ_L) and carrier (λ_C) contributions, and T is the temperature].[7] This has been attributed to its extraordinarily low thermal conductivity, which can be likened to a "phonon glass-electron crystal" thermoelectric property,[8] characteristic of an ideal thermoelectric material. Such exceptional low thermal conductivity is recognized originating at least in part from the complex and substantially disordered crystal structure with vacancies and interstitial Zn atoms,[9,10] or due to the low-frequency rattling motion of the Sb dimers in the crystal structure.[11]

Although thermoelectric performance of β-Zn_4Sb_3 is excellent in the moderate temperature range as compared to the other thermoelectric materials, its thermoelectric properties is still inadequate for practical use, and further improvement in its properties is vital for its application in large scale. In this aspect, many approaches to enhance ZT have been explored. Among them, doping has been widely studied to optimize the thermoelectric performance. For instance, dopants (metals) such as Pb, Bi, Mg, Cu, Co, Sn, In, Cd, Al, Ga, Nb, and Hg have been investigated so far.[12–23] The results have shown that upon doping with Sn, Cd, Nb, Co, or Cu, the high-temperature thermoelectric performance of Zn_4Sb_3 was improved greatly.[12–18] Unfortunately, low-temperature physical property measurements show that although the individual parameters are affected by doping, there is no overall improvement in the thermoelectric performance by far.[20–22] But our recent work reveals that a slight amount of Ag doping enhance the ZT by about 1.3 times as compared to undoped compound at room temperatures.[24] In view of the fact that Ag/Cu has fewer valence electrons than Zn, it is expected that an incorporation of Ag/Cu in β-Zn_4Sb_3 will increase hole concentration monotonically, which will cause electrical resistivity and Seebeck coefficients to decrease continually with increase in doping content. Nevertheless, contrary to one's expectation the low-temperature resistivity and Seebeck coefficients of Ag-doped β-Zn_4Sb_3 increase first and then decrease with increasing doping content, showing a nonmonotonic behavior.[24] In fact, metal doping in β-Zn_4Sb_3 can lead to consequences that are much more intricate than one would expect. For example, previous reports seem to indicate that metal doping can alter the Zn/Sb ratio of the bulk material and the subtle balance between Zn disorder and Zn deficiency in Zn_4Sb_3.[12,25] Consequently, carrier concentration and carrier dynamics are modulated correspondingly. Nevertheless, the detailed mechanism and criterion underlying remain unclear and intriguing. As a matter of fact, dopants can be incorporated in β-Zn_4Sb_3 in many ways: e.g., replace Zn and Sb from regular framework sites or replace interstitial Zn atoms. On the other hand, however, small concentration of the third metal component and the crystallographic problems associated with Zn disorder and structural complexity prohibit the extraction of conclusive results from x-ray diffraction (XRD) experiments.[25] Just as Nylén suggested, the consequences of metal doping to the structures of β-Zn_4Sb_3 and α-Zn_4Sb_3 are difficult to assess. Therefore, a combined study of theoretical calculations with experimental

measurements on the structural properties of metal-doped β-Zn_4Sb_3 system becomes imperative.

Based on our preliminary investigation on low-temperature thermoelectric properties of Ag-doped β-Zn_4Sb_3, in the present work we focused our attention on doping-content dependences of thermoelectric properties after doping of Ag and Cu in β-Zn_4Sb_3. Through combinations of experimental measurements with first-principles calculations and through comparison of Ag doping with Cu doping we tried to extract some important information which would help us to understand Ag and Cu doping and theirs effects on the thermoelectric properties of β-Zn_4Sb_3

II. EXPERIMENTAL AND COMPUTATIONAL METHODS

A. Materials synthesis and microstructure characterization

Ingots with nominal compositions of Zn_4Sb_3, $(Zn_{0.9975}Ag_{0.0025})_4Sb_3$, $(Zn_{0.995}Ag_{0.005})_4Sb_3$, $(Zn_{0.99}Ag_{0.01})_4Sb_3$, $(Zn_{0.9975}Cu_{0.0025})_4Sb_3$, $(Zn_{0.995}Cu_{0.005})_4Sb_3$, and $(Zn_{0.99}Cu_{0.01})_4Sb_3$ were synthesized by mixing appropriate stoichiometric ratios of high-purity starting elemental materials, namely, Zn, Sb, Ag, and Cu (>99.999% in purity). The corresponding elements were sealed in appropriate ratio in evacuated fused quartz ampules. The sealed ampules were heated to 1023 K and then held there for 12 h while rocking the liquid to facilitate complete mixing of the contents. Then the ampules were quenched in the water. The obtained ingots were ground in agate mortar to fine powders, which were then compacted (in a WC die) by hot pressing (under a pressure of 600 MPa) in vacuum at 573 K for 1 h to form bulk samples possessing good mechanical strength.

The phase structures of the obtained samples were determined by using XRD (Philips-X PERT PRO diffractometer) with Cu $K\alpha$ radiation (scan step size: 2θ=0.0176°, time per step: 19.685 s). Accuracy lattice parameters of β-$(Zn_{1-x}M_x)_4Sb_3$ (M=Ag,Cu) were measured with XRD by using a Si standard for calibration. The fracture surfaces were observed by using field emission scanning electron microscopy (FE-SEM, SIRION 200). The densities of the hot-pressed samples were measured in ethanol by using Archimedes method.

B. Measurements of thermoelectric properties

Electrical resistivity and Seebeck coefficients were measured simultaneously using a physical property measurement system (PPMS, Quantum Design). Electrical resistivity was measured with the four-probe method. Four probes (Cu straps) were electrically and thermally attached to the samples by silver conductive adhesive paste (Phentex Corp., Ward Hill, MA), and when Seebeck coefficients were measured the middle two probes were used to explore temperature gradient (difference) and potential difference. The Hall coefficients (R_H) were measured by applying a field of 0.73 T at room temperature (283 K), and the carrier concentration (p) was determined from the measured Hall coefficients.

C. First-principles calculations

Although β-Zn_4Sb_3 was already discovered in the late 1960s (Refs. 26–28) and subsequently structurally characterized,[29] a complete view on its true crystal structure was presented recently by Snyder *et al.* and Cargnoni *et al.*[9,10] through using the maximum-entropy method based on high-resolution synchrotron powder diffraction data. The crystal structure of a hypothetical disorder-free β-Zn_4Sb_3 has a framework $Zn_{12}Sb_{10}$, which contains three distinct atomic positions [36 Zn, 18 Sb(1), and 12 Sb(2) in space group $R\bar{3}c$] and can be described as consisting of channels formed by Zn and Sb(1) atoms running along the [001] direction. The chan-

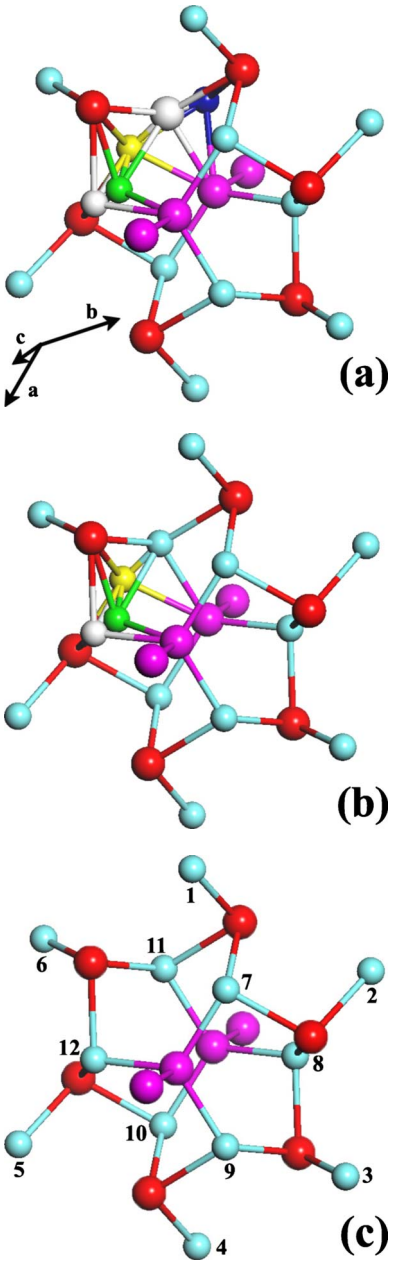

FIG. 1. (Color online) Crystal structures of the three primary unit cells (a) $A_{10}BCDSb_{10}$, (b) $A_{11}BCSb_{10}$, and (c) $A_{12}Sb_{10}$ representing β-Zn_4Sb_3 before relaxation. Sb(1) atoms [red (large black)]; Sb(2) atoms [pink (large dark gray)]; normal zinc atoms A (number 1–12) [cyan (small light gray)]; interstitial zinc atoms B [yellow (small gray)], C [green (small dark gray)], and D [blue (small black)]; and vacant zinc lattice sites V_1 (large white sphere) and V_2 (small white sphere).

nels are centered by chains of Sb(2) atoms, which are located on the threefold axes. Moreover, β-Zn_4Sb_3 manifests the disordering in the framework Zn position which displays a considerable occupational deficiency (0.89–0.90) and in the occurrence of three weakly occupied (by around 0.06) general positions representing interstitial Zn atoms. The expected ideal crystallographic composition of the so-called Zn_4Sb_3 is actually $Zn_{13}Sb_{10}$.[30] However, the actual composition of Zn_4Sb_3 obtained from the experimental refined occupancies should be expressed as $Zn_{13-\delta}Sb_{10}$ (δ=0.2–0.5),[30] a slight Zn deficiency with respect to $Zn_{13}Sb_{10}$. At around 254 K Zn-disordered β-Zn_4Sb_3 transforms into α-Zn_4Sb_3 where framework and interstitial Zn atoms order into distinct crystallographic sites. By comparing equivalent sections of the diamond-chain framework shown perpendicular to the channel direction for β-Zn_4Sb_3 and α-Zn_4Sb_3, Mikhaylushkin detected two five-atom clusters grouped together and related by a center of inversion in α-Zn_4Sb_3. And each pair of five-atom clusters replaces three pairs of Zn atoms from the regular diamond-chain framework.[31] Nylén pointed out that these missing pairs of Zn atoms are associated with the vacancies in β-Zn_4Sb_3.[25,30]

Obviously, both the dynamical disorder and a crystallographically variable Zn composition increase the complexity and difficulties in computer simulation. In other words, it is nearly impossible to theoretically simulate a truly practical structure of β-Zn_4Sb_3. However, one can use a reliable model to simplify practical structure of β-Zn_4Sb_3 so as to make the theoretical calculation feasible. For example, Cargnoni *et al.*[10] showed that the experimental stoichiometry $Zn_{12.816}Sb_{10}$ can be exactly reproduced by assuming that the material is a 0.184:0.420:0.396 mixture of $A_{12}Sb_{10}$, $A_{11}BCSb_{10}$, and $A_{10}BCDSb_{10}$ cells, where A, B, C, and D are the main Zn site (A) and three weakly occupied Zn interstitial sites (B, C, and D), respectively. In the proposed disorder models, one framework Zn atom is replaced by a pair of (B and C) interstitials ($A_{11}BCSb_{10}$ shown in Fig. 1), and a pair of framework Zn atoms is replaced by a triangle of interstitials B, C, and D ($A_{10}BCDSb_{10}$ shown in Fig. 1). It is recognized that these simple models are very reasonable when considering the α-Zn_4Sb_3 structure.[30] Hence, in the present work, we construct the three kinds of model unit cells of $A_{12}Sb_{10}$, $A_{11}BCSb_{10}$, and $A_{10}BCDSb_{10}$ (based on the experimental data presented in the literature of Ref. 10) as the initial input structures, shown in Fig. 1. Then we substituted Ag and Cu for each Zn site to obtain sixty defective configurations.

Our calculations were performed within the framework of the density-functional theory, with the PBE generalized gradient approximation to the exchange correlation energy, and the valence electron-ion interaction was modeled by the projector-augmented wave potential, as implemented in the Vienna *ab initio* simulation package (VASP).[32–34] The atoms of system were put in a unit cell with periodical boundary condition. The plane-wave cutoff and *k*-point density, obtained using the Monkhorst-Pack method, were both checked for convergence for each system to be within 0.001 eV/atom. Following a series of test calculations a plane-wave cutoff of 350 eV was adopted. The structural optimization was truncated when the forces converge to less than 0.01 eV/Å.

TABLE I. A list of densities, relative densities, and possible impurity phase related to the dopants for samples $(Zn_{1-x}M_x)_4Sb_3$ (M=Ag,Cu).

	x	Density (g cm^{-3})	Relative density (%)	Impurity phase
$(Zn_{1-x}Ag_x)_4Sb_3$	0	6.19	97.3	No
	0.0025	6.18	97.1	No
	0.005	6.19	97.4	No
	0.01	6.24	98.1	Ag_5Zn_8 (0.2 wt %)
$(Zn_{1-x}Cu_x)_4Sb_3$	0	6.19	97.3	No
	0.0025	6.19	97.3	No
	0.005	6.16	96.9	No
	0.01	6.22	97.8	No

Structural relaxations have been performed by using the conjugate gradient algorithm. The ionic coordinates and the unit-cell size and shape were optimized simultaneously to eliminate structures with internal stress. From the calculated total energies one can deduce the formation energies E_{form} of the various point defects defined as: (1) for dopants (Ag/Cu) filling vacancies,

$$E_{form} = E_{doped} - E_{undoped} - \mu_{Ag/Cu}, \quad (1)$$

(2) for dopants substituting for zinc atoms,

$$E_{form} = E_{doped} + \mu_{Zn} - E_{undoped} - \mu_{Ag/Cu}. \quad (2)$$

Here E_{doped} is the total free energy for the supercell containing the dopant (Ag/Cu), $E_{undoped}$ the total free energy for the undoped supercell, and μ is the chemical potentials of the constituent elements.

III. RESULTS AND DISCUSSIONS

A. Experimental results

1. Microstructural characterization

The densities of all the bulk samples used in present study were measured, and the obtained results were given in Table I. One can see that the relative densities of all the samples after hot pressing are around 97–98 % of the theoretical value (6.36 g cm^{-3}),[9,35] and the density differences among the samples with different doping content are usually not more than 1%, which ensures that the influences of microstructure differences (such as pores) among different doped samples on their transport and thermoelectric properties could be negligibly small. Moreover, FE-SEM observations were performed on the cross-section of the samples to examine qualities of the samples, and the result indicates that all the samples have high densification and only sparsely distributed micropores could be observed. As a typical example, Fig. 2 shows FE-SEM micrographs of the fracture surfaces for the hot-pressed samples β-$(Zn_{1-x}M_x)_4Sb_3$ (M=Ag,Cu) (x=0,0.01). One can see that only a very few of pores can be spotted on these fracture surfaces, indicating that the ob-

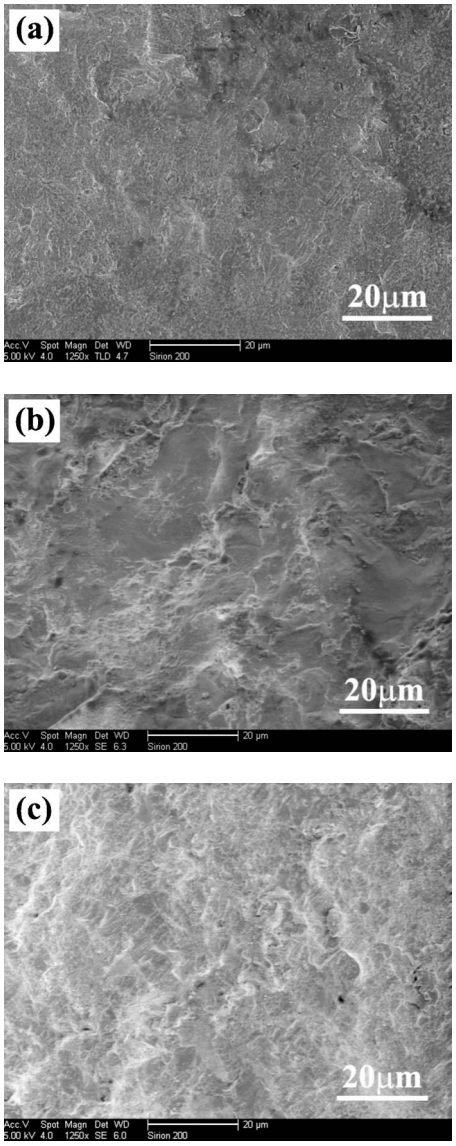

FIG. 2. FE-SEM micrographs of the fracture surfaces of samples (a) β-Zn_4Sb_3, (b) β-$(Zn_{0.99}Ag_{0.01})_4Sb_3$, and (c) β-$(Zn_{0.99}Cu_{0.01})_4Sb_3$.

tained samples are very dense. This result, in fact, is consistent with the result of our density measurements (Table I).

XRD patterns at room temperature of β-$(Zn_{1-x}M_x)_4Sb_3$ (M=Ag,Cu) (x=0,0.0025,0.005,0.01) samples were shown in Fig. 3. It can be seen that all main diffraction peaks for β-$(Zn_{1-x}M_x)_4Sb_3$ (M=Ag,Cu) (x=0,0.0025,0.005,0.01) correspond to β-Zn_4Sb_3 (Joint Committee for Powder Diffraction Standard No. 34-1013) phase with trigonal hexagonal lattice (space group $R\bar{3}c$). But through careful inspection, some additional weak peaks can also be identified in the XRD patterns for the samples, such as for β-$(Zn_{0.99}Ag_{0.01})_4Sb_3$ [as marked in pattern D of Fig. 3(a)] and β-$(Zn_{0.995}Cu_{0.005})_4Sb_3$ [as marked in pattern C of Fig. 3(b)]. Through analysis by Reitveld refinement, we find that all the samples contain a faint amount of ZnSb phase (usually much less than 1 wt %). The effects of this tiny amount of ZnSb phase on the electrical transport and thermoelectric properties among the compounds with different doping contents are expected to be negligibly small since its total content is very low as compared to the main phase (β-Zn_4Sb_3). For the sample β-$(Zn_{0.99}Ag_{0.01})_4Sb_3$, however, besides the additional diffraction peaks from ZnSb phase (~1.1 wt %), a trace of impurity- (dopant-) related phase Ag_5Zn_8 (~0.2 wt %) was detected [as marked in Fig. 3(a)], indicating that the solubility limit of Ag in β-Zn_4Sb_3 is less than that of Cu.

The variations in unit-cell parameters with doping content x for the β-$(Zn_{1-x}M_x)_4Sb_3$ (M=Ag,Cu) (x=0,0.0025,0.005,0.01) samples are shown in Fig. 4(a). As shown in Fig. 4(a), as doping content increases, the lattice parameters (a and c) increase monotonically, which indicates that dopants (Ag and Cu) are successfully introduced into the host, for Ag atom (atomic radius ~1.75 Å) or Cu atom (atomic radius ~1.57 Å) are larger than that of Zn atom (atomic radius ~1.53 Å), leading to expansion of the host lattice (β-Zn_4Sb_3). But it is not clear at this stage how Ag or Cu atoms are incorporated into β-Zn_4Sb_3. However, it is worthwhile to note that the observed evolution of lattice parameter ratio c/a for both Ag- and Cu-doped samples decreases monotonically with increase in doping content x, as shown in Fig. 4(b). It can be seen from this figure that as content x of Ag and Cu increases from 0 to 0.01, the ratio c/a decreases from 1.01695 to 1.01626 and 1.01677, respectively. The similar experimental result has been reported by Nakamoto *et al.*[20,36,37] in Cd-doped system, where the ratio c/a drops with the increase in Cd content. But the present result is opposite to the experimental data in In-doped system reported in our previous work.[20] This phenomenon cannot reasonably be explained by the difference in ionic radius (or covalent radius, even atom radius) between zinc and doping elements, but may be related to a specific occupation sites in the host, as mentioned previously.[20] However, the change behavior of ratio c/a could be served as a criterion for one to judge whether a given explanation could be consistent with the real physical events having happened in the system.

2. *Electrical resistivity and Seebeck coefficient*

The variations in electrical resistivity ρ and Seebeck coefficient S with temperature (in the range from 14 to 300 K) for $(Zn_{1-x}Cu_x)_4Sb_3$ (x=0,0.0025,0.005,0.01) were presented in Figs. 5(a) and 5(b), respectively. Similar to the Ag-doped compounds,[24] the resistivity and Seebeck coefficient generally increase with increasing temperature, exhibiting the behavior of a degenerated semiconductor. The observed anomalies in the plots of ρ-T and S-T for $(Zn_{1-x}Cu_x)_4Sb_3$ (x=0,0.0025,0.005,0.01) at around 260 K are associated with the structural transition from β to α/α' phase.[20,38,39] Specially, the resistivity and Seebeck coefficient of β-Zn_4Sb_3 (that is, at higher temperature range $T>$ ~260 K) change nonmonotonically with dopant content. For conciseness, Fig. 6 gives room-temperature (283 K) electrical resistivity of β-$(Zn_{1-x}M_x)_4Sb_3$ (M=Ag and Cu) as a function of doping content x. One can see that as x increases from 0 to 0.0025, the resistivity ρ of β-$(Zn_{1-x}Ag_x)_4Sb_3$ increases remarkably from 3.18×10 to 5.77×10^{-5} Ω m. However, with further increase in x ρ de-

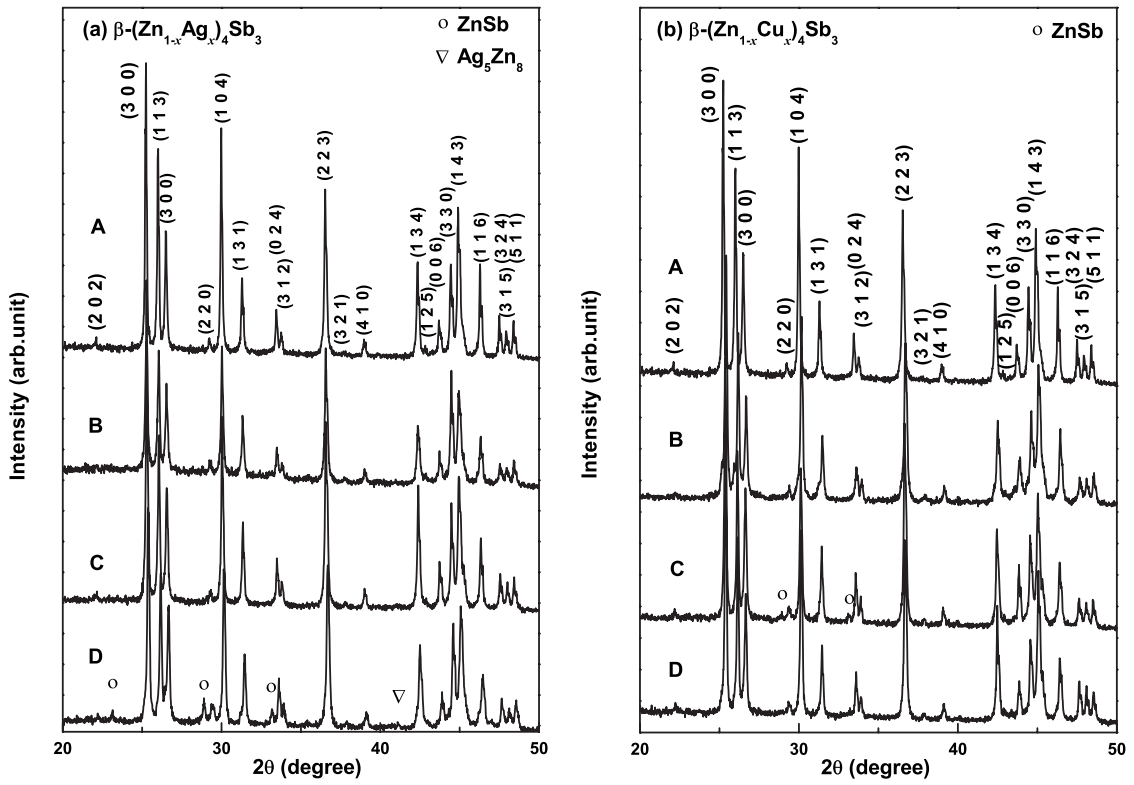

FIG. 3. XRD patterns of (a) β-$(Zn_{1-x}Ag_x)_4Sb_3$ and (b) β-$(Zn_{1-x}Cu_x)_4Sb_3$. (A) $x=0$; (B) $x=0.0025$; (C) $x=0.005$; and (D) $x=0.01$.

creases dramatically to 2.90×10^{-5} Ω m, which is even smaller than that of β-Zn_4Sb_3. The room-temperature resistivity (3.18 mΩ cm) of β-Zn_4Sb_3 obtained here is larger than that (2 mΩ cm) reported by Caillat *et al.*[7] for their β-Zn_4Sb_3. Such a difference may arise from either the differences in microstructures (such as differences in grain sizes, and residual (micro) pores and their shape as well as their distributions) or/and carrier concentrations (see following text) of the samples obtained under different fabrication conditions. The dependence of the resistivity on doping content for Cu-doped samples is basically similar to that of β-$(Zn_{1-x}Ag_x)_4Sb_3$. However, one obvious difference from Ag doping lies in the fact that the decrease in the resistivity with doping content defers substantially, where ρ does show any decrease until $x>0.005$ (Fig. 6).

Figure 7 shows room-temperature Seebeck coefficients of β-$(Zn_{1-x}M_x)_4Sb_3$ as a function of doping content. The positive values of the Seebeck coefficients of the samples mean that the major charge carriers in all the samples are holes. By comparing Fig. 7 with Fig. 6 one can find that the change in Seebeck coefficient of β-$(Zn_{1-x}M_x)_4Sb_3$ with doping content has similar behavior to that of the resistivity, increasing first and then decreasing at the corresponding doping contents. It is worthwhile to point out that this nonmonotonic change behavior of resistivity and Seebeck coefficient is reproducible in different batches of samples (with the same nominal compositions) prepared in the same conditions. Hence, this phenomenon strongly suggests that the changes in both resistivity and Seebeck coefficients originate from a same physical mechanism. In order to understand the change behavior of the resistivity and Seebeck coefficient of

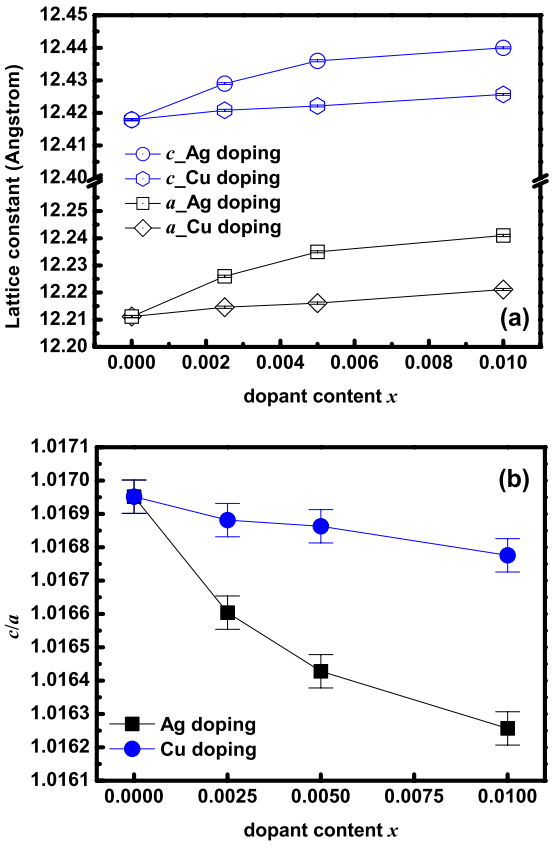

FIG. 4. (Color online) Variation in (a) lattice constants a and c and (b) their ratio c/a of β-$(Zn_{1-x}M_x)_4Sb_3$ [M=Ag (from our early work, Ref. 23) and Cu] with Ag/Cu concentration x.

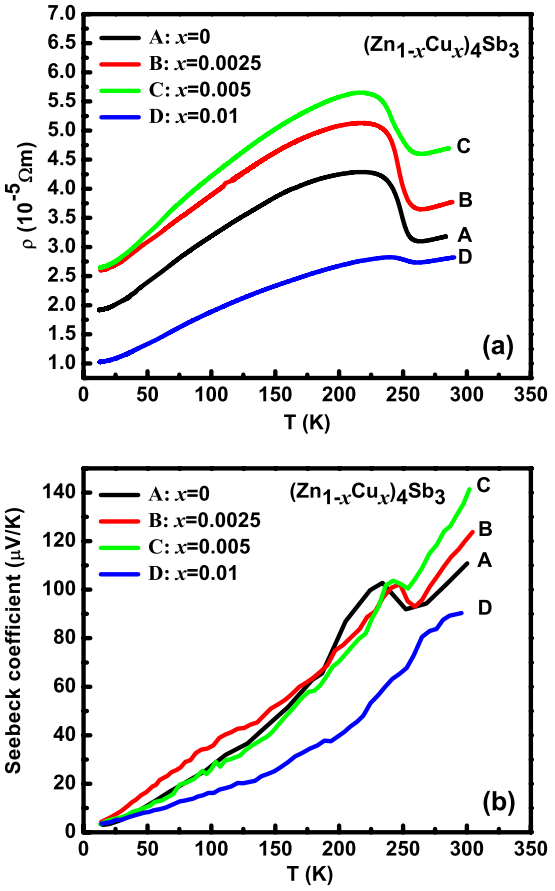

FIG. 5. (Color online) Temperature dependence of the (a) electrical resistivity and (b) Seebeck coefficient for $(Zn_{1-x}Cu_x)_4Sb_3$.

β-$(Zn_{1-x}M_x)_4Sb_3$, carrier (hole) concentration as a function of doping content was determined by the measurements of Hall coefficients. It is worth noting here that the carrier concentration (as shown in Fig. 8) of undoped β-Zn_4Sb_3 obtained here (3.3×10^{19} cm^{-3}) is comparable to the result (3×10^{19} cm^{-3}) obtained by Bhattacharya *et al.*;[40] but it is obviously smaller than the value (9×10^{19} cm^{-3}) reported by Caillat *et al.*[7] This difference would be related to the specific

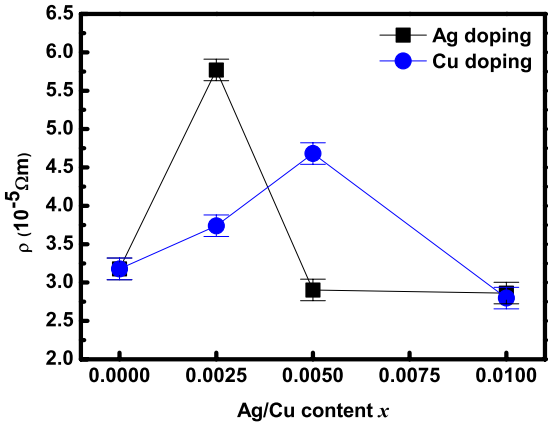

FIG. 6. (Color online) Variation in the room-temperature electrical resistivity of β-$(Zn_{1-x}M_x)_4Sb_3$ (M=Ag,Cu) as a function of Ag/Cu concentration x.

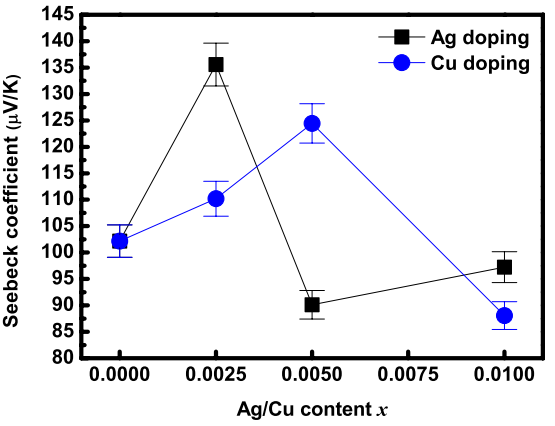

FIG. 7. (Color online) Variation in the room-temperature Seebeck coefficient of β-$(Zn_{1-x}M_x)_4Sb_3$ (M=Ag,Cu) as a function of Ag/Cu concentration x.

fabrication conditions (e.g., different cooling rate in quenching the samples, leading to different interstitial Zn atoms contained) realized by different groups. Furthermore, it can be seen from Fig. 8 that as x increases from 0 to 0.0025, the hole concentration of β-$(Zn_{1-x}Ag_x)_4Sb_3$ decreases from 3.3×10^{19} to 2.2×10^{19} cm^{-3}, and then increases to 4.7×10^{19} cm^{-3} with x further increasing to 0.005. Likewise, the hole concentration of β-$(Zn_{1-x}Cu_x)_4Sb_3$ decreases from 3.3×10^{19} to 2.7×10^{19} cm^{-3} with increasing x from 0 to 0.005, and then increases sharply to $\sim4.0\times10^{19}$ cm^{-3} at x =0.01. In addition, the carrier mobility of the samples was estimated based on the data of the resistivity and carrier concentration, which indicates carrier mobility μ is 56.8 $cm^2/V\,s$, 48.9 $cm^2/V\,s$, 42.8 $cm^2/V\,s$, and 50.3 $cm^2/V\,s$, respectively, for β-$(Zn_{1-x}Ag_x)_4Sb_3$ (x=0,0.0025,0.005,0.01); while the mobility is 56.8 $cm^2/V\,s$, 53.0 $cm^2/V\,s$, 49.1 $cm^2/V\,s$, and 54.9 $cm^2/V\,s$, respectively, for β-$(Zn_{1-x}Cu_x)_4Sb_3$ (x=0,0.0025,0.005,0.01). This indicates that carrier mobility basically decreases after doping due to enhanced impurity (dopants) scattering; besides, the carrier mobility in Ag-

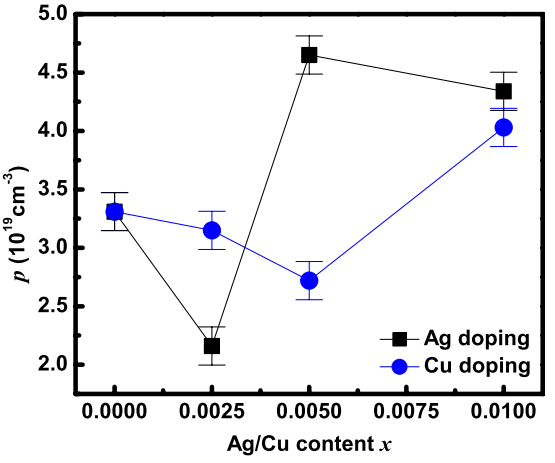

FIG. 8. (Color online) Variation in the room-temperature carrier concentration p of β-$(Zn_{1-x}M_x)_4Sb_3$ (M=Ag,Cu) as a function of Ag/Cu concentration x.

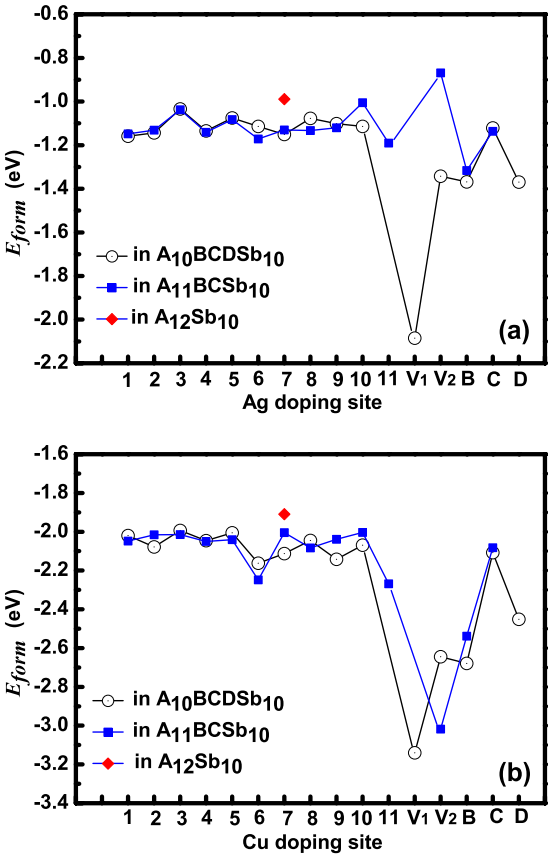

FIG. 9. (Color online) Formation energies (E_{form}) of Ag/Cu defects in the framework of $A_{10}BCDSb_{10}$, $A_{11}BCSb_{10}$, and $A_{12}Sb_{10}$. The abscissa represents different zinc sites (numbers denote different Zn atoms in normal lattice sites, as labeled in Fig. 1) occupied by dopants (a) Ag and (b) Cu.

doped compounds is generally smaller than that in Cu-doped compounds presumably due to large lattice distortion caused by larger atomic radius of silver. However, it is worthwhile to point out that the estimated mobility here is an apparent mobility that is influenced sensitively by microstructures (such as porosities) of the consolidated samples, implying that detail comparison among the samples with different dopant contents is hardly meaningful. Therefore, present results demonstrate that the nonmonotonic changes in both the resistivity and Seebeck coefficients with doping content are mainly caused by nonmonotonic change in carrier concentration in β-$(Zn_{1-x}M_x)_4Sb_3$. Nevertheless, why the carrier concentration of β-$(Zn_{1-x}M_x)_4Sb_3$ changes nonmonotonically with doping content is elusive, which is a key issue for one to understand doping mechanism of Ag/Cu and their effects on the thermoelectric properties of β-Zn_4Sb_3.

B. Calculation results

In order to help us understand above results observed in Ag- and Cu-doped β-Zn_4Sb_3, first-principles calculations were carried out on doping of Ag/Cu in β-Zn_4Sb_3. The obtained formation energies (E_{form}) of Ag/Cu doping at different sites in the frameworks of $A_{10}BCDSb_{10}$, $A_{11}BCSb_{10}$, and $A_{12}Sb_{10}$ are shown in Fig. 9. Here, the calculated chemical potentials of the constituent elements μ of Zn, Ag, and Cu are −0.164 eV, −0.205 eV, and −0.066 eV, respectively. One can see from Fig. 9(a) that the formation energy of Ag substitution for normal lattice Zn is around −1.1 eV in average in the structures of both $A_{11}BCSb_{10}$ and $A_{10}BCDSb_{10}$, which is obviously lower than that of substitution in $A_{12}Sb_{10}$ structure. In comparison, Ag atom filling V_1 in $A_{10}BCDSb_{10}$ has a lowest E_{form}=−2.1 eV. Then, Ag atom filling V_2 or replacing B and D interstitial atoms in $A_{10}BCDSb_{10}$ have relatively low E_{form} (around −1.4 eV). In contrast, in structure $A_{11}BCSb_{10}$ the lowest E_{form} (around −1.3 eV) corresponds to Ag substitution for interstitial B. Surprisingly, however, as Ag atom filling V_2 in $A_{11}BCSb_{10}$ has a maximum E_{form}. Therefore, a comparison of the formation energies of Ag-doped systems among different doping sites indicates that Ag atom will preferentially fill the vacancy V_1 (see Fig. 1) and then will replace interstitials D and B (in both $A_{10}BCDSb_{10}$ and $A_{11}BCSb_{10}$) and V_2 (only in $A_{10}BCDSb_{10}$).

Figure 9(b) shows formation energies for Cu doping at different Zn sites. It can be seen that E_{form} of Cu substitution for normal lattice Zn is around −2.1 eV in average in both $A_{11}BCSb_{10}$ and $A_{10}BCDSb_{10}$, which is not only lower than that of substitution in $A_{12}Sb_{10}$ structure but also obviously lower than that of Ag substitution in all of the corresponding sites. Cu atom filling vacancy V_1 in $A_{10}BCDSb_{10}$ has a lowest E_{form}=−3.14 eV. As Cu fill the vacancy V_2 and replace interstitials B and D in $A_{10}BCDSb_{10}$, E_{form} are −2.65 eV, −2.68 eV, and −2.45 eV, respectively. In contrast to Ag doping in $A_{11}BCSb_{10}$, Cu filling vacancy V_2 here has a lowest energy E_{form}=−3.02 eV (this difference is expected to be related to the difference in atomic radius between Ag and Cu), where the second lowest E_{form}=−2.54 eV for Cu replacing interstitial B. Hence, a comparison of the formation energies of Cu-doped system among different doping sites would tell us that Cu atom will preferentially occupy the vacant zinc lattice sites V_1 and V_2 (see Fig. 1) in the structure of $A_{10}BCDSb_{10}$, and it will also occupy the vacancy V_2 in $A_{11}BCSb_{10}$. Among the interstitial sites Cu atom will preferentially replace B and D in the framework of $A_{10}BCDSb_{10}$ and B in the framework of $A_{11}BCSb_{10}$.

The lattice constants a and c of Ag-/Cu-doped systems are calculated and the ratio c/a is given in Fig. 10 as a function of doping site. One can see from Fig. 10(a) that the ratio c/a changes with doping sites and has a maximum in the case of Ag filling V_2. Nevertheless, we know experimentally that after Ag/Cu doping the ratio c/a decreases invariably. This means that one should exclude those doping sites that are even energetically favored but whose c/a ratios possess a higher value than that of undoped one. In other words, low formation energy E_{form} is only a necessary condition but not a sufficient condition. Based on this criterion, among the possible doping sites in Ag-doped system only doping at V_1, D, and B sites in the framework of $A_{10}BCDSb_{10}$ as well as B site in the framework of $A_{11}BCSb_{10}$ have smaller c/a than their initial values, and they are optional doping sites depending on their energy values. Similarly, one can see from Fig. 10(b) that among the possible doping sites in Cu-doped system, only doping at V_1, V_2, and B sites in the framework of $A_{10}BCDSb_{10}$ as well as B site in the framework of $A_{11}BCSb_{10}$ have smaller c/a than their initial values, and

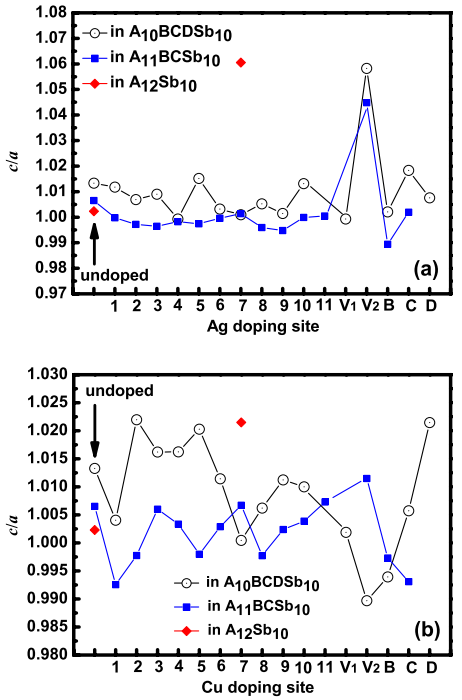

FIG. 10. (Color online) The theoretical calculated ratios of lattice constants c/a for Ag-/Cu-doped defective configurations in the framework of $A_{10}BCDSb_{10}$, $A_{11}BCSb_{10}$, and $A_{12}Sb_{10}$. The abscissa represents different zinc sites (numbers denote different Zn atoms in normal lattice sites, as labeled in Fig. 1) occupied by dopants (a) Ag and (b) Cu.

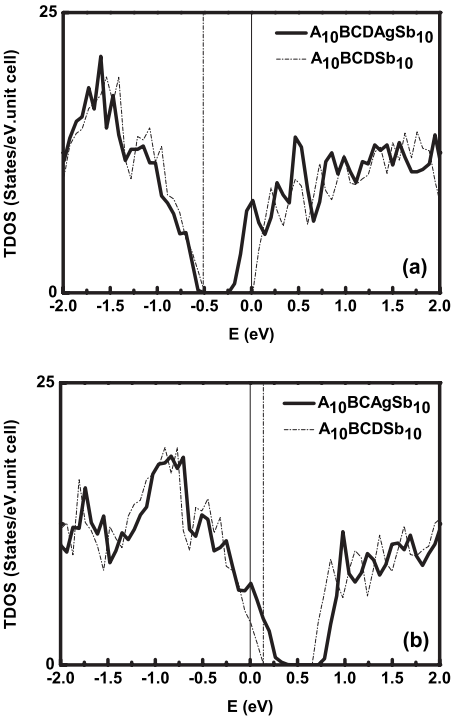

FIG. 11. TDOS of defective configurations (a) with Ag filling vacancy V_1 and (b) with Ag replacing interstitial Zn atom D in the framework of $A_{10}BCDSb_{10}$, where the Fermi-energy level is set at zero. For comparison, the TDOS and Fermi-energy level of undoped $A_{10}BCDSb_{10}$ are shown in dashed.

therefore they are optional doping sites depending on their energy values. Comparing Cu-doped system with Ag-doped system, a striking difference one finds is that Ag can hardly occupy vacancy V_2 in either $A_{10}BCDSb_{10}$ (though having lower energy but large ratio c/a) or $A_{11}BCSb_{10}$ (having both higher energy and larger ratio c/a), which would be related to its larger atomic radius. Moreover, the formation energies of Cu doping at almost all the sites are substantially smaller in magnitude than those of Ag doping. This suggests that Cu can be dissolved into β-Zn_4Sb_3 with a greater amount. Table II lists longest (Ll) and shortest (Ls) bond lengths around Ag/Cu atom doping at several representative sites in Ag-/Cu-doped system after relaxation.

From the results outlined above we know that Ag/Cu doping in β-Zn_4Sb_3 can be generally classified as both filling normal Zn lattice vacancies (i.e., V_1 and V_2) and substitution for interstitial Zn atoms (such as B and D) in frameworks of $A_{10}BCDSb_{10}$ or/and $A_{11}BCSb_{10}$. The effects of Ag/Cu filling Zn lattice vacancies on their electronic structures are expected to be different from those of Ag/Cu substitution for interstitial Zn atoms. Therefore, the electronic structure calculations were carried out for each case. As a typical example, Figs. 11 and 12 give the total densities of states (TDOS) of Ag-doped framework $A_{10}BCDSb_{10}$ and Cu-doped $A_{10}BCDSb_{10}$, respectively. In order to observe easily the effects of the Ag/Cu doping, the TDOS of the undoped system was also plotted for comparison. As shown in Fig. 11(a), Ag filling vacancy V_1 introduces considerable states near the bottom of conduction band (CB) of $A_{10}BCDSb_{10}$, which extend nearly 0.26 eV into the band gap. Ag and its nearest-neighbor Sb and Zn atoms have the highest contribution to

TABLE II. A list of the Ll and Ls bond lengths around Ag/Cu atom doping at different sites in Ag-/Cu-doped systems after relaxation. (Annotation: the symbol for the defects in Table II is universally expressed as M_n, where M stands for doping elements (Ag or Cu) and the subscript n denotes doping sites. For instance, Ag_{V_1} represents the defect of Ag occupying vacancy V_1.)

	Defect type	Ll (Å)	Ls (Å)	Defect type	Ll (Å)	Ls (Å)
$A_{10}BCDSb_{10}$	Ag_{V_1}	3.298	2.674	Cu_{V_1}	2.714	2.508
	Ag_D	3.046	2.658	Cu_B	2.690	2.536
$A_{11}BCSb_{10}$	Ag_{V_2}	2.920	2.614	Cu_{V_2}	2.616	2.418
	Ag_B	2.904	2.677	Cu_B	2.664	2.534

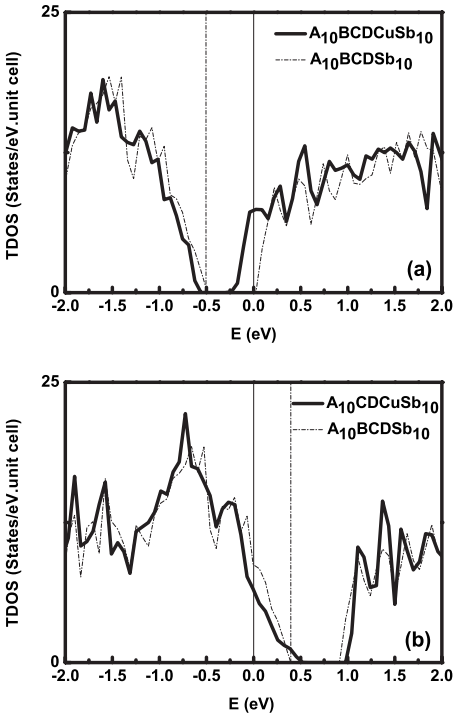

FIG. 12. TDOS of defective configurations (a) with Cu filling vacancy V_1 and (b) with Cu replacing interstitial Zn atom B in the framework of $A_{10}BCDSb_{10}$, where the Fermi-energy level is set at zero. For comparison, the TDOS and Fermi-energy level of undoped $A_{10}BCDSb_{10}$ are shown in dashed line.

these states. The Ag *d* states hybridize with Sb *p* states and Zn *s* states in the range (0.26, 0.52) eV. Therefore, these states are not only resonant[41] with the CB of $A_{10}BCDSb_{10}$ but also they extend into the gap of $A_{10}BCDSb_{10}$. On the other hand, Ag replacing interstitial D introduces states near the top of the valence band (VB) of $A_{10}BCDSb_{10}$ [Fig. 11(b)]. Partial DOS analysis (not shown here) indicates that these states consist mostly of *p* orbital of Sb and Zn atoms which are the nearest neighbors of Ag. These states extend into the gap region and reduce the band gap of $A_{10}BCDSb_{10}$.

Results for Cu doping are similar to those of Ag doping in the sense that Cu in vacancy V_1 introduces new states near bottom of CB; whereas Cu replacing interstitial B site introduces new states near the top of VB [Figs. 12(a) and 12(b)], decreasing the band gap of $A_{10}BCDSb_{10}$. Both Ag- and Cu-doped compounds show semiconducting behavior with a very smaller gap and with a substantially increased TDOS near CB and VB extremes as compared to the TDOS of $A_{10}BCDSb_{10}$. Moreover, it is found that the Fermi level shifts toward the CB of undoped structures when Ag/Cu filling vacancy V_1, which indicates that Ag/Cu acts as donors, resulting in the decrease in hole concentration of the doped compound; while when Ag/Cu replaces interstitial sites D or B the Fermi level shifts into the deep of VB, which means that Ag/Cu plays the role of an acceptor, giving rise to an increase in the hole concentration.

However, it is worthwhile to point out here that our calculated DOS for Ag-/Cu-doped frameworks (such as $A_{10}BCDSb_{10}$) should exaggerate significantly doping effects on the DOS due to much higher doping concentration in calculation than that in practically synthesized samples. For instance, in the case of Ag/Cu filling vacancy V_1 Fermi level shifts into CB [Figs. 11(a) and 12(a)], which will not take place [instead, Fermi level is expected to shifts slightly toward CB] in real system due to very lightly doping in experiments. Similarly, the magnitude of the shift for Fermi level after Ag/Cu replacing interstitials D and B should be much smaller than that in the lightly doped real system. But, the calculation results obtained here are expected to be qualitatively consistent with real physical events (or processes) having happened in the doped compounds. This means that the variation trend of hole concentration and transition of the doping role from donor to acceptor for Ag/Cu at different kinds of doping sites are reliable. In fact, our calculation results can give a reasonable explanation to experimental results obtained in the present study. According to the conclusions of formation energy E_{form}, Ag/Cu will preferentially fill vacancy V_1 due to its lowest E_{form}, resulting in a decrease in hole concentration (Fig. 8) and giving rise to an increase in the resistivity and Seebeck coefficients (Figs. 6 and 7). Since the number of the vacancy V_1 is very limited in real samples, substitution of Ag/Cu for interstitial Zn atoms (i.e., D and B) will become dominant as doping content increases, which would lead to a increase in hole concentration (Fig. 8), as manifested by the decrease in the electrical resistivity and Seebeck coefficients at higher doping concentration (Figs. 6 and 7).

In addition, in contrast to Ag that can only fill in vacancy V_1, Cu atoms can not only fill vacancy V_1 but also fill vacancy V_2. This will cause the transition of doping role of Cu from donor to acceptor to delay as compared to Ag, which could reasonably account for why the increase in hole concentration and decrease in the resistivity and Seebeck coefficients of β-$(Zn_{1-x}Ag_x)_4Sb_3$ occur at the doping content $x=0.0025$, which is postponed to $x=0.005$ for β-$(Zn_{1-x}Cu_x)_4Sb_3$. Moreover, one knows from Figs. 9 and 10 that the number of possible Cu-filled vacancies is more than that of Ag doing and E_{form} for Cu doping is almost always substantially lower than that for Ag doping at corresponding sites, implying that the host can accommodate more Cu atoms, which could explain why the solubility of Cu is higher than that of Ag in β-Zn_4Sb_3, as observed experimentally (Fig. 3).

IV. CONCLUSIONS

We have studied the effects of doping of Ag or Cu on structural and thermoelectric properties of β-Zn_4Sb_3 theoretically as well as experimentally. The results indicate that the resistivity and Seebeck coefficients of β-$(Zn_{1-x}M_x)_4Sb_3$ (M = Ag, Cu) increase and then decrease with the increasing dopant content, which is consistent with the nonmonotonous change behavior of the carrier concentration. First-principles calculations show that Ag will first fill the vacancy V_1 (refer Fig. 1) and then will incorporate into interstitial sites D and B in the framework of $A_{10}BCDSb_{10}$ or interstitial site B in the framework of $A_{11}BCSb_{10}$ based on the differences in formation energies. In contrast, Cu atoms could occupy not

only V_1 but also V_2 in the framework of $A_{10}BCDSb_{10}$. When Ag and Cu occupy the vacancies, Fermi levels shift toward conduction band, signifying a decrease in hole concentration and acting as donors. On the contrary, Ag and Cu substituting for the interstitial atoms (D or B) causes the Fermi levels to shift toward the deep of valence band, indicating an increase in hole concentration and serving as acceptors. In addition, Cu doping always has lower energies of defect formation and more vacancies to be occupied than Ag, which could give a reasonable explanation for the higher solubility of Cu than for Ag in β-Zn_4Sb_3.

ACKNOWLEDGMENTS

This work was supported by the National Natural Science Foundation of China (Grants No. 10774145, No. 50701043, No. 10904144, and No. 50972146) and the Center for Computational Science, Hefei Institutes of Physical Sciences.

*Corresponding author; xyqin@issp.ac.cn

[1] B. C. Sales, D. Mandrus, and R. K. Williams, Science **272**, 1325 (1996).
[2] R. Venkatasubramanian, E. Siivola, T. Colpitts, and B. O'Quinn, Nature (London) **413**, 597 (2001).
[3] G. Mahan, B. Sales, and J. Sharp, Phys. Today **50** (3), 42 (1997).
[4] T. M. Tritt, Science **272**, 1276 (1996).
[5] T. M. Tritt, Science **283**, 804 (1999).
[6] F. J. DiSalvo, Science **285**, 703 (1999).
[7] T. Caillat, J.-P. Fleurial, and A. Borshchevsky, J. Phys. Chem. Solids **58**, 1119 (1997).
[8] Y. Wu, J. Nylén, C. Naseyowma, N. Newman, F. J. Garcia-Garcia, and U. Häussermann, Chem. Mater. **21**, 151 (2009).
[9] G. J. Snyder, M. Christensen, E. Nishibor, T. Caillat, and B. B. Iversen, Nature Mater. **3**, 458 (2004).
[10] F. Cargnoni, E. Nishibori, P. Rabiller, L. Bertini, G. J. Snyder, M. Christensen, C. Gatti, and B. B. Iversen, Chem.-Eur. J. **10**, 3861 (2004).
[11] W. Schweika, R. P. Hermann, M. Prager, J. Perßon, and V. Keppens, Phys. Rev. Lett. **99**, 125501 (2007).
[12] A. P. Litvinchuk, J. Nylén, B. Lorenz, A. M. Guloy, and U. Häussermann, J. Appl. Phys. **103**, 123524 (2008).
[13] T. Koyanagi, K. Hino, Y. Nagamoto, H. Yoshitake, and K. Kishimoto, 16th International Conference on Thermoelectrics, 1997, p. 463.
[14] T. Caillat and J.-P. Fleurial, Proc. IEEE **2**, 905 (1996).
[15] K.-W. Jang, I.-H. Kim, J.-I. Lee, and G.-S. Choi, 24th International Conference on Thermoelectrics, 2005, p. 129.
[16] J. L. Cui, L. D. Mao, D. Y. Chen, X. Qian, X. L. Liu, and W. Yang, Curr. Appl. Phys. **9**, 713 (2008).
[17] J. L. Cui, H. Fu, D. Y. Chen, L. D. Mao, X. L. Liu, and W. Yang, Mater. Charact. **60**, 824 (2009).
[18] D. Li, H. H. Hong, J. Ma, and X. Y. Qin, J. Mater. Res. **24**, 430 (2009).
[19] F. Liu, X. Y. Qin, and D. Li, J. Phys. D **40**, 4974 (2007).
[20] G. Nakamoto, T. Souma, M. Yamaba, and M. Kurisu, J. Alloys Compd. **377**, 59 (2004).
[21] B. L. Pedersen, H. Birkedal, E. Nishibori, A. Bentien, M. Sakata, M. Nygren, P. T. Frederiksen, and B. B. Iversen, Chem. Mater. **19**, 6304 (2007).
[22] B. L. Pedersen, H. Birkedal, M. Nygren, P. T. Frederiksen, and B. B. Iversen, J. Appl. Phys. **105**, 013517 (2009).
[23] F. Liu, X. Y. Qin, and H. X. Xin, J. Phys. D **40**, 7811 (2007).
[24] L. Pan, X. Y. Qin, M. Liu, and F. Liu, J. Alloys Compd. **489**, 228 (2010).
[25] J. Nylén, S. Lidin, M. Andersson, H. Liu, N. Newman, and U. Häussermann, J. Solid State Chem. **180**, 2603 (2007).
[26] Y. A. Ugai, E. M. Averbakh, and V. V. Lavrov, Sov. Phys. Solid State **4**, 2393 (1963).
[27] V. I. Psarev and N. L. Kostur, Izv. Vyssh. Uchebn. Zaved. Fiz. **10**, 34 (1967).
[28] Y. A. Ugai, T. A. Marshakova, V. Y. Shevchenko, and N. P. Demina, Inorg. Mater. **5**, 1381 (1969).
[29] H. W. Mayer, I. Mikhail, and K. J. Schubert, J. Less-Common Met. **59**, 43 (1978).
[30] J. Nylén, S. Lidin, M. Andersson, B. B. Iversen, H. Liu, N. Newman, and U. Häussermann, Chem. Mater. **19**, 834 (2007).
[31] A. S. Mikhaylushkin, J. Nylén, and U. Häussermann, Chem.-Eur. J. **11**, 4912 (2005).
[32] P. E. Blöchl, Phys. Rev. B **50**, 17953 (1994).
[33] G. Kresse and D. Joubert, Phys. Rev. B **59**, 1758 (1999).
[34] J. P. Perdew, K. Burke, and M. Ernzerhof, Phys. Rev. Lett. **77**, 3865 (1996).
[35] V. Izard, M. C. Record, J. C. Tedenac, and S. G. Fries, CALPHAD: Comput. Coupling Phase Diagrams Thermochem. **25**, 567 (2001).
[36] V. L. Kuznetsov and D. M. Rowe, J. Alloys Compd. **372**, 103 (2004).
[37] T. Souma and M. Ohtaki, J. Alloys Compd. **413**, 289 (2006).
[38] T. Souma, G. Nakamoto, and M. Kurisu, J. Alloys Compd. **340**, 275 (2002).
[39] T. Souma, G. Nakamoto, and M. Kurisu, Proceedings of the 20th International Conference on Thermoelectrics, 2001, p. 274.
[40] S. Bhattacharya, R. P. Hermann, V. Keppens, T. M. Tritt, and G. J. Snyder, Phys. Rev. B **74**, 134108 (2006).
[41] D. Bilc, S. D. Mahanti, K.-F. Hsu, E. Quarez, R. Pcionek, and M. G. Kanatzidis, Phys. Rev. Lett. **93**, 146403 (2004).